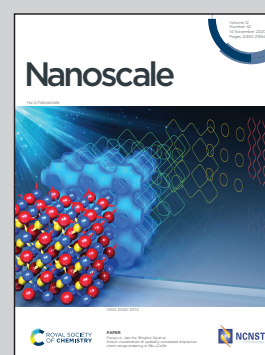Showcasing research from Prof. Calderón's group at POLYMAT - Basque Center for Macromolecular Design and Engineering, Spain and from Strumia's group at National University of Córdoba, Argentina.

Revealing the NIR-triggered chemotherapy therapeutic window of magnetic and thermoresponsive nanogels

The combination of magnetic nanoparticles and thermoresponsive nanogels was explored as an effective strategy for the development of theranostic nanogels. These hybrid nanomaterials showed outstanding properties for magnetic resonance imaging and triggered release of encapsulated cargoes. *In vivo* experiments demonstrated their capacity as nanocarriers for near-infrared (NIR) triggered chemotherapy and highlighted the relevance of the correct concentration/dose in this antitumoral modality to achieve a superior therapeutic efficacy.

As featured in:

ROYAL SOCIETY
OF **CHEMISTRY**

rsc.li/nanoscale

Registered charity number: 207890

PAPER

Check for updates

Revealing the NIR-triggered chemotherapy therapeutic window of magnetic and thermoresponsive nanogels†

Catalina Biglione, [ID] ‡[a,b,c] Julian Bergueiro, [ID] ‡[a,d] Stefanie Wedepohl, [ID][a]
Bastian Klemke, [ID][e] Miriam C. Strumia [ID] *[b,c] and Marcelo Calderón [ID] *[a,f,g]

The combination of magnetic nanoparticles and thermoresponsive nanogels represents an appealing strategy for the development of theranostic probes. These hybrid nanocarriers present several advantages such as outstanding properties for guided therapy, magnetic resonance imaging, and triggered release of encapsulated cargoes. Most magnetic thermoresponsive nanogels are built with strategies that comprise a physical interaction of particles with the polymeric network or the covalent attachment of a single particle to the linear polymer. Herein, we report a facile synthetic approach for the synthesis of magnetic and thermoresponsive nanogels that allows the controlled incorporation of multiple superparamagnetic inorganic cores as covalent cross-linkers. An ultrasonication-assisted precipitation–polymerization afforded nanogels with sizes in the nanometric range and similar magnetization and light transduction properties compared to the discrete magnetic nanoparticles. The theranostic capability of these nanocarriers was further investigated both *in vitro* and *in vivo*. *In vivo* experiments demonstrated the capacity of these materials as nanocarriers for near-infrared (NIR) triggered chemotherapy and highlighted the relevance of the correct concentration/dose in this antitumoral modality to achieve a superior therapeutic efficacy.

Introduction

Smart nanogels have become materials of remarkable importance in nanomedicine due to their attractive capabilities of responding to different external stimuli.[1–3] In particular, because of their versatility, the use of thermoresponsive nanogels in different biomedical applications such as drug delivery,

theranostics, and tissue engineering have recently gained interest.[4–6] Considering the outstanding properties of nanogels like superior biocompatibility, high loading capacity, passive targeting, *etc.*, nanogels have been the focus of continuous research for developing superior drug delivery systems.[7] In this regard, there is an increasing interest in the incorporation of triggers able to respond to external stimuli for clinical anti-cancer applications.[8–10] The incorporation of photo-transducers, which are able to convert near-infrared (NIR) radiation in the so-called biological window (wavelengths between 700 and 1000 nm) into heat, within the nanogel structure is of high interest for remote triggering.[11,12] This non-invasive NIR radiation can be used to remotely generate a controlled amount of heat that can lead to the collapse of the nanogel's thermo-responsive polymer network, thus triggering the release of encapsulated drugs. This remotely triggered delivery strategy takes advantage of the deep penetration of NIR laser light into tissues and reduces the undesired non-selective heating and ablation of healthy tissues.[13–16]

Therefore, the choice of the photo-transducer building block in the construction of a smart nanodevice is crucial to the system's efficiency and applicability. Organic dyes,[17] conducting polymers,[18] and anisotropic gold nanoparticles[19] have been widely utilized for this purpose. In this regard, iron oxide magnetic nanoparticles (MNPs) present several advantages

[a]Freie Universität Berlin, Institute of Chemistry and Biochemistry, Takustrasse 3, 14195 Berlin, Germany
[b]Departamento de Química Orgánica, Facultad de Ciencias Químicas, Universidad Nacional de Córdoba, Av. Haya de la Torre esq. Av. Medina Allende, Córdoba, Argentina. E-mail: mstrumia@unc.edu.ar
[c]Instituto de Investigación y Desarrollo en Ingeniería de Procesos y Química Aplicada (IPQA), CONICET. Av. Velez Sárfield 1611, Córdoba, Argentina
[d]Centro Singular de Investigación en Química Biolóxica e Materiais Moleculares (CIQUS), Departamento de Química Orgánica, Universidade de Santiago de Compostela, 15782 Santiago de Compostela, Spain
[e]Helmholtz-Zentrum Berlin für Materialien und Energie GmbH, Hahn-Meiter Platz 1, 14109 Berlin, Germany
[f]POLYMAT and Applied Chemistry Department, Faculty of Chemistry, University of the Basque Country UPV/EHU, Paseo Manuel de Lardizabal 3, 20018 Donostia-San Sebastián, Spain. E-mail: marcelo.calderon@polymat.eu
[g]IKERBASQUE, Basque Foundation for Science, 48013 Bilbao, Spain
†Electronic supplementary information (ESI) available. See DOI: 10.1039/d0nr02953j
‡Both authors contributed equally to this work.

that makes them perhaps the best choice as phototransducers: (a) they are capable of transducing NIR light into heat,[20,21] (b) MNPs also generate heat when excited with an alternating magnetic field,[22–25] (c) their paramagnetic properties make them optimal candidates for magnetic resonance imaging (MRI) contrast agents,[26–29] and (d) magnet guided therapy can be performed with these systems as well.[30–33]

Because of the above-mentioned reasons, many efforts have been focused on the development of magnetic and thermo-responsive nanogels (MNGs).[34–36] A variety of approaches that use non-covalent interactions have been considered for the incorporation of MNPs into a nanogel's polymeric matrix. These range from a simple mixture of MNPs and nanogel suspensions[20,32,37] to the *in situ* synthesis of nanogels in the presence of a solution of MNPs,[35,38,39] or *vice versa* by the *in situ* synthesis of MNPs in a nanogel dispersion.[40,41] However, the non-covalent incorporation methods have important drawbacks like the desorption of the MNPs or the aggregation of the particles inside the nanogels that affects both the magnetic properties of the composites and the drug loading capacity of the systems.

To overcome this disadvantage, MNPs can be incorporated using covalent chemistry, thus allowing a more controlled and stable union. The inherent aggregation of the MNPs, however, makes the task of controlling the incorporation of the particles in the polymer network challenging, as is reflected in the few reports in the literature.[42,43] The need for new approaches to overcome the actual disadvantages of using magnetic hybrid systems is therefore evident.

Hence, we decided to investigate a novel strategy with the potential to bring the control over the discrete incorporation of MNPs into a thermoresponsive nanogel network. We target this new approximation to create a more advanced remotely triggered drug delivery system. The construction of a nanogel with dispersed magnetic particles on its polymer network will allow: (a) fixing the magnetic cores in the interior of the nanogel *via* a covalent bonding, avoiding particle aggregation or loss; (b) maintaining the phototransducing properties of discrete MNPs; (c) keeping magnetic properties close to the ones of the MNPs; and (d) enhancing the hydrophobic drug encapsulation capacity by maximizing the available MNP hydrophobic surface.

In our synthetic approach, MNPs are used as cross-linkers in the synthesis of oligoethylene glycol (OEG)-based nanogels. The novel robust strategy for the synthesis of thermoresponsive magnetic nanogels (MNGs) described here is based on ultrasound-assisted precipitation–polymerization. Furthermore, the obtained MNGs were fully characterized and their *in vitro* and *in vivo* applications as potential theranostic agents were assessed.

Materials and methods

Materials

All chemicals were purchased from Merck and Acros Organics and used as received. Doxorubicin hydrochloride was pur-chased from Yick-Vic Chemicals & Pharmaceuticals. Water used for the experiments was obtained from a Millipore water purification system (18.2 MΩ cm).

Methods

Synthesis of magnetic nanoparticles. The synthesis of iron oxide MNPs was carried out by the coprecipitation of iron salts.[44] Briefly, $FeCl_3 \cdot 6H_2O$ (16.136 g) and $FeCl_2 \cdot 4H_2O$ (5.556 g) were placed in a 250 mL round bottom flask together with 130 mL of Milli-Q water. 70 mL of NH_4OH (3 M) was added dropwise and left under magnetic stirring for 15 minutes. Then, the nanoparticles were magnetically separated, and the supernatant discarded. The MNPs were resuspended in 20 mL of HNO_3 (2 M) and stirred for a further 15 minutes. To purify the MNPs, they were washed with acetone (2x) and water (1x) using magnetic separation.

Surface modification of the MNPs with the methacrylate moieties (MNP@MEMO). To perform the surface functionali-zation of the nanoparticles, we followed the protocol pre-viously developed.[31] Briefly, 50 mg of MNPs were suspended in 26 mL of an $EtOH : H_2O$ (1 : 1) mixture. Then 2 mL of 3-(meth-acryloyloxy)propyl trimethoxysilane (MEMO) was added and the resulting dispersion was sonicated 5 times for 2 minutes with an ultrasonicator (70% power, Bandelin UW 2070 or Omni-Ruptor 400 tip sonicator). The reaction mixture was purified with magnetic separation and washed 3 times with acetone. Finally, MNP@MEMO were resuspended in Milli-Q water.

Synthesis of magnetic thermoresponsive nanogels (MNGs). Generally, diethylene glycol methacrylate (DEGMA, 0.8 mmol), oligoethylene glycol methacrylate (OEGMA, 0.2 mmol) mono-mers, HEMA (4 mol%), sodium dodecyl sulfate (SDS, 1.6 mol%) and ammonium persulfate (APS, 0.8 mol%) were placed in a flask with 10 mL of distilled water. Then, 1.5 mg of MNP@MEMO and N,N,N',N'-tetramethylethylenediamine (TEMED, 0.3 mL, 0.25 M) were added. The solution was heated to 60 °C. The reaction mixture was ultrasonicated discontinu-ously (6 times) at 70% of power for 15 minutes (70% power, Omni-Ruptor 400 or Bandelin UW 2070 sonicator). The nano-gels were purified by magnetic separation and subsequent dialysis against water for 3 days at room temperature using a 50 kDa MWCO membrane. Different screening parameters were studied such as the amount of MNP@MEMO, DEGMA : OEGMA ratio, *etc*. (see Table 1).

Infrared spectroscopy (FT-IR). Transmittance and reflectance IR studies were carried out using either a JASCO FT-IR 4100 spectrophotometer or an FT-IR NICOLET IN microscope in the range of 4000–500 cm^{-1} with a resolution of 4 cm^{-1} and 32 scans.

Dynamic light scattering (DLS). DLS experiments were carried out using a Malvern Zetasizer Nano-ZS 90 (Malvern Instruments), equipped with a He–Ne laser (λ = 633 nm) and a dispersion angle of 173°. Particle sizes and size distribution were obtained from the average of 3 measurements of intensity distribution curves.

Nanoparticle tracking analysis (NTA). NTA experiments were performed on a Malvern NanoSight NS500 device equipped

Table 1 MNG reaction conditions and size (DLS) and thermoresponsivity characterization (turbidimetry)

Batch	Molar ratio DEGMA : OEGMA[a]	MNP@MEMO (mg)	Diameter (nm)	SD (nm)	T_{CP} (°C)
MNG1	0.8 : 0.2	0.6	650	225	46
MNG2		1.5	210	5	47
MNG3		2.3	277	11	47
MNG4		3.0	222	3	52
MNG5	1 : 0	1.5	185	46	30
MNG6	0.95 : 0.05		355	92	36
MNG7	0.9 : 0.1		286	19	40
MNG8	0.7 : 0.3		253	2	60

[a] HEMA (4 mol%), SDS (1.6 mol%), APS (0.8 mol%), TEMED (0.3 mL, 0.25 M) and water (10 mL).

with a SCMOS camera and with a 635 nm laser under a dispersion angle of 100° to 25°. Video capture was performed with a camera level, a sliding shutter and a slip gain set to 13, 800 and 350, respectively. For each sample 3 video frames were recorded for 30 seconds with 25 FPS. Data analysis was performed using NTA 3.0 0064 software.

Transmission electron microscopy (TEM). Transmission and scanning electron microscopy samples were prepared by blotting samples on carbon-coated copper grids (300 mesh, QUANTIFOIL, Grosslöbichau, Germany) and visualized using the TEM detector on a Hitachi scanning electron microscope (SU8030, Hitachi, Tokyo, Japan) at 20–30 kV and 10 µA. A 0.03 mg mL^{-1} solution of each nanoparticle was employed in the measurements.

Thermogravimetric analysis (TGA). Thermogravimetric analysis of the samples (1–10 mg) was performed on a Shimadzu DTG-60 (Japan) analyzer. The measurement was performed at temperatures ranging from 25 to 800 °C at a heating rate of 10 °C min^{-1} under N$_2$ atmosphere.

NIR irradiation experiments. 200 µL of MNG solution were placed in a PCR tube and irradiated with a 785 nm laser (500 mW, 0.59 W cm^{-2}) for 10 min to reach the plateau temperature. The temperature was monitored with an FLIR E4 thermal camera (FLIR Systems GmbH, Frankfurt, Germany). Each experiment was performed in triplicate and Milli-Q water was used as blank. Different MNG concentrations were evaluated.

Magnetization experiments. Magnetization measurements were performed at the Quantum Materials CoreLab at the Helmholtz-Zentrum Berlin using a Magnetic Property Measurement System (5T-MPMS, Quantum Design) equipped with a superconducting quantum interference device (SQUID) magnetometer. The magnetization of the magnetic nanogels (powder, 4 mg) was measured in the field range from −20 000 to 20 000 Oe and at different temperatures.

Magnetic resonance imaging (MRI). Prior to the measurements, MNGs in different concentrations were fixed in 1% agarose gel. T_2-Weighted images and T_2 relaxation times were acquired using a Bruker 7T BioSpec (Bruker, Germany) with a 20 mm-Quadrature-Volume Resonator (Rapid Biomed). The T_2-weighted images were acquired using conventional spin echo acquisition techniques (TR = 2000 ms) with TE values ranging from 6 to 260 ms. The relaxivities, r_2, were calculated from the

curve fit of the T_2 measured relaxation rates ($\Delta R_2 = 1/T_{2background} - 1/T_2$, s^{-1}) as a function of the iron concentration (mM).

Deprotonation of Dox·HCl. For the deprotonation of doxorubicin hydrochloride, 400 mg of Dox·HCl (0.690 mmol) were dissolved in 400 mL Milli-Q H$_2$O in a 1 L separatory funnel. Then, 200 mL of dichloromethane (DCM) and 4 mL of trimethylamine (TEA) were added. The organic layer was separated, and the aqueous layer was washed again 6 times with 200 mL of fresh DCM. The combination of the organic layers was dried with anhydrous sodium sulfate and filtered. The solvents were removed under high vacuum to ensure the complete disappearance of TEA.

Drug encapsulation. For the incorporation of doxorubicin, 1 mL of an aqueous solution of MNG (2 mg mL^{-1}) was mixed in 1 mL of Dox in THF at different concentrations (*e.g.* 1, 2, 3, and 4 mg mL^{-1}) and incubated for 16 h under mechanical agitation at room temperature. Then, the MNGs were magnetically separated from the solution and washed twice with water. The remaining solution of each wash was quantified using UV-vis spectrophotometry. The absorption was measured at 480 nm to calculate the efficiency of encapsulation and loading of the drug. For this, a Dox·HCl calibration curve was previously performed in THF to obtain the molar absorptivity coefficient. Each experiment was performed in triplicate.

Drug release. To perform doxorubicin release assays, 10 samples of 100 µL of an MNG-DOX in solution (2 mg mL^{-1}) at different pH values (4.2, 5.0, 6, and 7.4) were prepared. All samples began the release at the same time under mechanical agitation, but each sample was separated at different times. The system was separated by a magnetic field and the remaining solution was quantified by UV-vis spectrophotometry. Absorbance at 480 nm was measured to calculate the percentage of release. These tests were performed at 37 and 50 °C. Each experiment was performed in triplicate. For the release studies triggered by NIR light, a similar protocol was followed, but after 12 h, the samples were irradiated for 5 minutes with a 785 nm laser (500 mW, 0.59 W cm^{-2}). The UV spectra of the supernatant were recorded before and after the irradiation.

Cell culture. HeLa cells (Leibniz Institute DSMZ – German Collection of Microorganisms and Cell Cultures GmbH #ACC 57) were routinely cultured in RPMI 1640 medium (Gibco, Thermo Fisher Scientific) containing 10% FBS (Biowest), 1%

penicillin/streptomycin (Gibco, Thermo Fisher Scientific) and 1% non-essential amino acid solution (Gibco, Thermo Fisher Scientific) at 37 °C and 5% CO_2.

MTT test. 10 000 HeLa cells per well were seeded into 96 well plates and grown over night. The next day, the cells were treated with fresh medium containing different 10-fold serial dilutions of the MNGs and incubated for 48 h. The medium was removed and the cells were washed twice with 200 μL per well PBS. 10 μL per well MTT solution (5 mg mL^{-1} in PBS, Sigma) in 100 μL per well fresh medium was added to the wells and incubated for 4 h at 37 °C. The supernatant was discarded afterwards, and formazan crystals were solubilized by adding 100 μL per well isopropanol containing 0.04 M HCl. Absorbance at 570 nm was read in an Infinite M200 Pro microplate reader (Tecan). Relative viabilities were calculated by dividing the absorbance values of wells containing treated cells divided by the values of untreated cells (100%). The assay was performed in duplicate and repeated 3 times independently.

In vitro photothermal therapy. 10 000 HeLa cells were seeded into 96 well plates and grown over night. The next day, the cells were treated with different amounts of MNGs, MNG-Dox or mixtures of both. For this, the MNGs were centrifuged, resuspended in a cell culture medium and added to the wells. The plate was placed onto a magnet plate fitted to 96 well plates to concentrate the particles on the surface of the cells. The plate was placed under an NIR lamp (Hydrosun® 750) and illuminated for 5 minutes. The plates were returned to the incubator for 24 h. Afterwards, the cell viability was determined by CellTiter-Glo® Luminescent Cell Viability Assay (Promega), according to the instructions of the manufacturer. Briefly, 100 μL of CellTiter-Glo® Reagent was added to each well, mixed for 2 minutes, and the lysates were transferred to a white 96-well plate. After 10 minutes of signal stabilization at room temperature, the luminescence was read in an Infinite M200 Pro microplate reader (Tecan), and relative viability values were calculated using the signals of untreated cells as reference.

Determination of the maximum tolerated dose (MTD). All animal procedures were performed in accordance with national and local guidelines and regulations for care and use of laboratory animals as described in Tierversuchsantrag G 0030/15 and approved by Landesamt Berlin für Gesundheit on 20.09.2018 for EPO GmbH Berlin-Buch. During all studies, the behavior of the mice was monitored regularly as an indicator for the tolerability of the treatments and to ensure that the animals did not feel pain or endure stress. Female NMRI nu/nu mice were treated with single doses of 10, 20, 40, 70, and 100 mg kg^{-1} MNG by intravenous administration through the tail vein and the toxicity and tolerability were monitored by body weight changes and behavioural indications. The maximum tolerated dose of 100 mg kg^{-1} was then injected daily for five consecutive days. The mice were observed for another 15 days. Afterwards, the mice were sacrificed and the organs (the spleen, kidneys, liver, heart, and lungs) were collected and prepared for histopathological examination. For

this, paraformaldehyde-fixed, paraffin-embedded organ blocks were cut into sections and stained with hematoxylin and eosin. In addition, the biodistribution was measured using MRI as described above.

In vivo MNG accumulation in tumor. Female NMRI nu/nu mice were injected with 1×10^7 A549 cells subcutaneously. The mice were injected intravenously through the tail vein with a single dose of 100 mg kg^{-1}, once the xenograft tumors reached about 100 mm^3 (~day 7 after inoculation). A single dose of doxorubicin (8 mg kg^{-1}) served as a control. Different groups of mice (n = 3 mice per group) were sacrificed after 2 h, 6 h, 12 h, 24 h and 48 h and the tumors were collected for analysis.

In vivo photothermal tumor therapy. Female NMRI (nu/nu) mice bearing A549 xenograft tumors were randomly distributed into different groups (n = 5 mice per group). When the tumor size reached 80–100 mm^3, a single dose of 100 mg kg^{-1} MNG or MNG-Dox was injected intravenously through the tail vein. 12 h after injection, the tumors were irradiated for 5 minutes with an NIR laser (785 nm, 500 mW). To compare the different application routes, the other groups of mice were treated with injections of 46 μL of a 16 mg mL^{-1} MNG or MNG-Dox dispersion directly into the tumor and the tumors were irradiated 5 minutes after intratumoral injection for 5 minutes as for the other groups as mentioned before. Tumor volume and body weight was monitored until day 38, after which the mice were sacrificed, and the tumors were collected and weighed.

Results and discussion

MNG synthesis

To covalently introduce MNPs into the polymeric network of nanogels, we propose a facile method inspired by our previously reported ultrasound-assisted precipitation–polymerization.[45] This strategy presents several advantages such as short reaction times, no necessity for an inert atmosphere, and low polydispersity of the formed nanogels. More importantly, the use of ultrasonication guarantees the colloidal stability of the MNPs during the synthesis, which ensures an even distribution of the inorganic cores in the network. In our strategy, the MNGs will be composed of two main building blocks:

(a) MNPs as cross-linking blocks. MNPs decorated with methacrylate moieties on their surface were synthesized by the functionalization of bare MNPs—spherical nanoparticles with an average diameter of 10 ± 3 nm (Fig. S1 and 2†) constructed with (trimethoxysilyl)propyl methacrylate (MEMO), as reported earlier.[44] This functionalization was performed by an improved ultrasonication-based method previously reported by our group and it afforded MEMO-coated MNPs (MNP@MEMO) with similar size and dispersity as the bare ones.[31] The functionalization was confirmed by the appearance of the signal characteristic of silane at 1200 cm^{-1} in Fourier transform infrared spectroscopy (FT-IR) (Fig. S1†) and scanning and transmission electron microscopy (SEM and TEM) (Fig. S2†).

(b) Thermoresponsive polymeric network. Commercially available oligoethylene glycol methacrylate (OEGMA) can be polymerized in a simple and versatile manner. Their principal advantage is that the system's cloud point temperature (T_{CP}) can be regulated with precision by changing the ratio between monomers with long and short pendant chains.[46] Apart from this, the resulting polymers present attractive properties such as high colloidal stability in water, biocompatibility, thermosensitivity, *etc.*[47–50] Moreover, thermoresponsive nanogels can be synthesized with control over their size that allowed their use in passive targeting modalities for tumor accumulation, taking advantage of the well-known enhanced permeability and retention effect (EPR).[16,18,51] The combination of crosslinked OEG polymers with non-covalently entrapped MNPs has been reported with promising properties in theranostic devices for controlled drug delivery and magnetic hyperthermia.[52–59] Nevertheless, to the best of our knowledge, no report regarding the properties of these types of systems as phototransducers have been published so far. Moreover, we incorporated a hydrophilic monomer, 2-hydroxyethyl methacrylate (HEMA), to minimize the impact on the hydrophobic–hydrophilic balance of the resulting system.

To overcome all intrinsic problems of MNPs in the synthesis methodologies, we have utilized a precipitation–polymerization strategy that involves ultrasonication assistance. The use of ultrasound has two reasons: (a) on the one hand, as we had reported,[45] it affects directly the seeding process of precipitation–polymerization, giving a superior control over the size of the formed nanogels and (b) on the other hand, it guarantees a good dispersion of the magnetic particles that tend to easily aggregate during the nanogel formation process.

This new approach in the synthesis of MNGs allows us not only to evenly distribute the MNPs in the polymer network but also to achieve control over both the size and transition temperature.

First, we analyzed the influence of the amount of inorganic cross-linkers in the MNG synthesis on the size and cloud point temperature (T_{CP}) of the nanogels. We kept a molar ratio of 0.8 : 0.2 (DEGMA : OEGMA) constant and varied the amounts of the MNPs from 0.6 to 3 mg (Table 1). The size of the MNGs determined using dynamic light scattering (DLS) was around 200 nm for all MNP@MEMO amounts but for the lower amount, 0.6 mg, larger sizes of 650 nm with a large standard deviation (Fig. 1B and Table 1) were observed. Regarding the thermoresponsiveness of the MNGs, we determined the T_{CP} with turbidimetry and found values around 46 °C for MNGs with 0.6 to 2.3 mg of MNP@MEMO and a T_{CP} of 52 °C for MNGs with 3 mg. Thus, only the incorporation of amounts higher than 2.3 mg of magnetic nanoparticles per batch had an influence on the thermoresponsive behaviour of the nanogels. Hence, MNGs with 1.5 mg of MNP@MEMO showed a better balance of incorporation of magnetic particles and less aggregation and were therefore chosen for further studies. A more in-depth study on the size of the selected MNGs was performed. A size distribution analysis of TEM images revealed a mean diameter of 99.2 nm and PDI of 0.24 (Fig. 1D, Fig. S3 and S4†). These smaller diameter values are expected since the nanogels collapse in the dry conditions that electron microscopy techniques require.

The influence of the molar ratio between DEGMA : OEGMA on thermoresponsiveness was assessed by keeping the amount of MNP@MEMO constant (1.5 mg). All resulting nanogels presented sizes between 200 and 300 nm without a clear trend (Fig. 1C). The colloidal stability of the system decreased with increasing the DEGMA feed ratio as reflected by the SD (Table 1). Contrarily, the T_{CP} values showed a clear tendency:
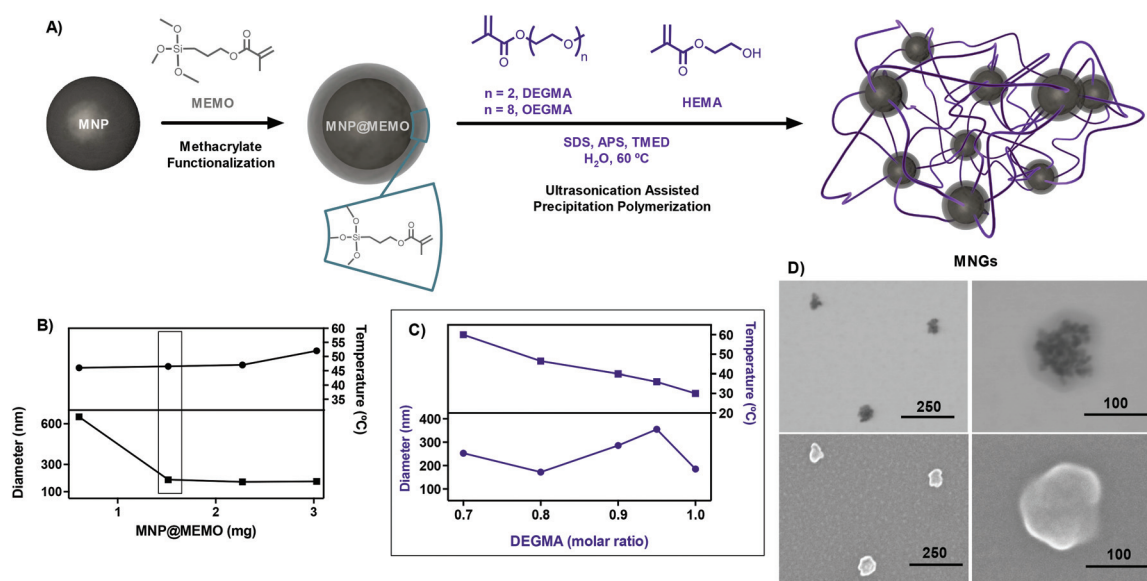

Fig. 1 (A) Synthesis of MNP@MEMO and MNG. Influence of (B) MNP@MEMO amounts, and (C) DEGMA molar ratio on the size and T_{CP} of the resulting MNGs. (D) TEM and SEM micrographs of the MNGs. The scale bars denote nm.

as the amount of the hydrophobic monomer (DEGMA) increased, the T_{CP} decreased, which is in concordance with the literature.[60] Therefore, we could fine-tune the T_{CP} values into the relevant range for biomedical applications.

Conditions of molar ratio 0.8 : 0.2 DEGMA : OEGMA with 1.5 mg of MNP@MEMO were chosen due to their size (210 nm) (Fig. S5†), a T_{CP} of 46 °C (Fig. S6†), and colloidal stability, fulfilling the requirements of a NIR-triggered drug delivery device. The successful incorporation of magnetic particles into the MNGs under these synthetic conditions was confirmed by FT-IR (Fig. S7†). The disappearance of the double bond conjugated with the carbonyl group between 1685 and 1665 cm^{-1} indicated the successful polymerization. In addition, the presence of the characteristic bands at 2925 cm^{-1} and 2869 cm^{-1} (C–H aliphatic stretching), at 1728 cm^{-1} (C=O stretching, esters) verified the polymer structure of the MNGs. Moreover, thermal gravimetric analysis (TGA) revealed that, while the bare MNPs and MNP@MEMO had only marginal weight loss, the MNGs suffered a significant loss (56.2 wt%), which can be attributed to the polymer network and the rest arising from the inorganic material (43.8 wt%) (Fig. S8†).

The size and morphology of the system was studied under diluted conditions with nanoparticle tracking analysis (NTA) finding similar hydrodynamic sizes as with DLS (Fig. S9†). Transmission and scanning electron microscopy (TEM/SEM) images confirmed the morphology of the hybrid nanogels (Fig. 1D) as having a globular shape and a high number of MNPs distributed in polymeric material.

The dispersions of the MNGs had high colloidal stability compared to other magnetic systems (greater than 6 months, Fig. S5†) and the nanocarriers could be easily isolated with a magnet (Fig. S10†). In case of any aggregation that could be observed at high concentrations, the system can be easily redispersed by mild sonication. To confirm their superparamagnetic properties, magnetization measurements were performed in the presence of an external field at different temperatures (27, 37, 45, and 50 °C). The superparamagnetic behaviour was demonstrated since no hysteresis cycles were observed at any of the temperatures studied (Fig. 2A). A comparison of MNP@MEMO and MNGs (normalized to the inorganic weight content, 43.8%) (Fig. S11†) revealed a negligible loss of magnetization properties. This supports the fact that the use of MNPs as covalent crosslinkers in the gel network prevents their aggregation and their magnetic properties almost remain intact. As the system contains a thermosensitive polymer that may change the proximity between the magnetic cores, we studied the effect of the temperature on the magnetic behaviour (Fig. 2B). We observed that the magnetization decreases linearly with the temperature as expected, and the magnetization was not affected near the T_{CP} of the system.

In order to demonstrate the potential of the nanogels as MRI contrast agents, we characterized the relaxation times of the nanogels using a magnetic resonance imaging (MRI) scanner (Fig. 2C). The MNGs presented similar transversal relaxation times (r_2) comparable to commercially available con-
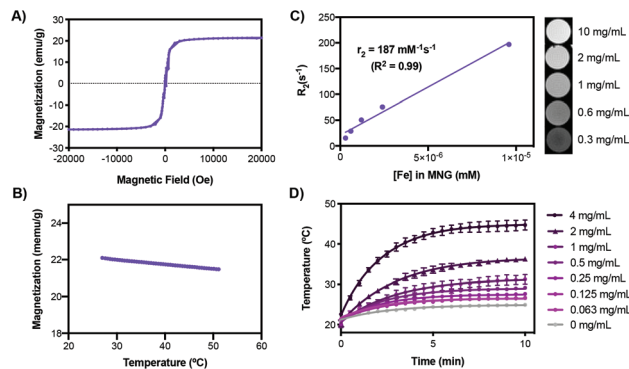

Fig. 2 (A) Magnetization curve of the MNGs at 27 °C. (B) Magnetization of the MNGs at 10 000 Oe with increasing temperature. (C) T_2-Weighted MRI images and MRI transverse relaxation times of the MNGs at different concentrations. (D) Heating curves under 10 minutes of NIR laser irradiation of the MNGs at different concentrations.

trast agents (187 mM^{-1} s^{-1}), highlighting the potential of these hybrid systems as theranostic probes.[61]

The capacity of MNPs to transduce heat from NIR light and consequently their applications in photothermal therapy has been reported.[35,62,63] Hence, we tested the photothermal conversion capability of the nanogels under irradiation with NIR light. For this, we placed small volumes of the MNGs at different concentrations in a PCR tube and irradiated from above with a 785 nm laser (500 mW, 0.59 W cm^2) continuously for 10 min. The temperature was monitored with a thermal camera during the whole experiment. A concentration-dependent heat generation capacity was found of 5 °C for the most dilute solution (0.063 mg mL^{-1}) and a maximum of 22 °C for the highest concentration (4 mg mL^{-1}) reaching a temperature of 46 °C (Fig. 2D). In addition, we analyzed the photothermal capacity of MNP@MEMO. To compare both systems, we studied the temperature increase at different concentrations of the inorganic material. For this, we normalized the MNG data to the iron oxide nanoparticle content (Fig. S12†). While comparing the values, it can be demonstrated that at the same amount of phototransducer, MNP@MEMO, similar heating curves were observed. Therefore, we could prove the capacity of MNGs to act as phototransducers and that the nanogel network does not interfere in the heating capacity of the magnetic nanoparticles.

Doxorubicin encapsulation and release studies

With the purpose of studying the capacities of these materials as nanocarriers, we selected doxorubicin (Dox) as an anticancer model drug. We studied the encapsulation efficiency (EE) of the MNGs using different concentrations of Dox. Encapsulation efficiencies close to 30% were reached at Dox concentrations ranging from 1 to 4 mg mL^{-1}. The drug loading content (DLC) in the systems was between 15 and 40% (Fig. 3B and C). These values are close to and even higher than those that can be found in the literature for similar systems.[52,58] This fact could be attributed to the nature of the
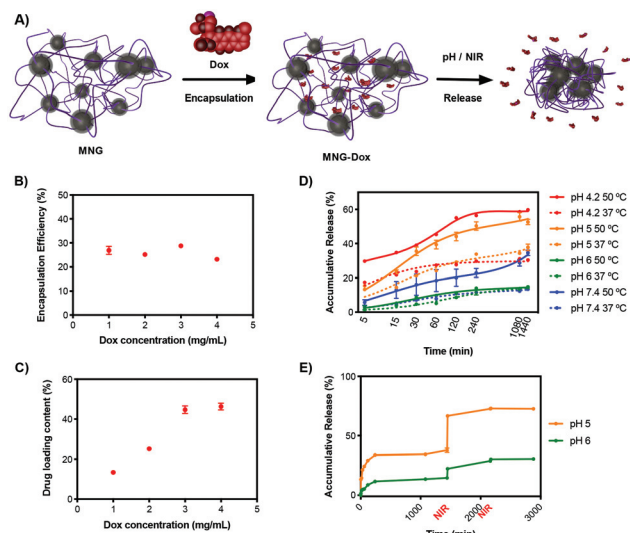
Fig. 3 (A) Schematic representation of doxorubicin load and triggered release from the MNGs. (B) Drug loading content and (C) encapsulation efficiency at different Dox concentrations. (D) Release studies at different pH values and temperatures. (E) NIR-triggered release studies (time in log scale).

hybrid system in which MNPs are not aggregated and which allows a higher incorporation of the hydrophobic drug.

We evaluated the drug release under different conditions such as pH, temperature, and NIR irradiation using nanogels of 40% DLC (Fig. 3D). In acidic medium (pH 4.2 and 5), Dox-loaded magnetic nanogels (MNG-Dox) showed an enhanced release compared to higher pH values like 6 or 7.4. This enhancement can be explained by considering the fact that Dox can be protonated at acidic pH, gaining hydrophilicity and thus being released from the hydrophobic domains of the hybrid network. Moreover, we investigated the influence of the thermoresponsive behaviour of the nanogels on Dox release. As expected, a temperature above the T_{CP} of the nanogels (46 °C) resulted in an increased release from 25% to 60% at pH 4.2. This perfectly fits our application rationale of enhancing the release in an acidic tumor microenvironment.[64] To analyze the mechanism of drug release, the data obtained were fitted with the most relevant kinetic models for drug release: zero-order, first-order, Higuchi, Korsmeyer–Peppas and Hixon–Crowell release models.[65] For all the experiments, the model with the highest R^2 was considered as the best fit of the release data. The analysis of the release kinetics revealed that most probably the drug release follows the Korsmeyer–Peppas model (Fig. 3D and Table S1†), which is expected since this model is an equation to describe drug release from polymeric systems.[66]

To confirm that Dox release can be triggered by NIR-induced temperature increase and subsequent collapse of the network, we irradiated the MNG solution for 5 minutes with an NIR laser (785 nm, 500 mW, 0.59 W cm^2) at pH 5 and 6 and measured the release after 12 hours. In both cases, we observed that the release can be boosted by 35% (pH 6) and

60% (pH 5) by NIR irradiation (Fig. 3E). However, a second NIR irradiation did not affect the release profile, indicating that the maximum release was achieved with a single irradiation of 5 min.

NIR-triggered chemotherapy evaluation *in vitro*

The ability of nanogels to perform as theranostic probes clearly depends on factors such as their cytotoxicity, their cancer cell killing capacity, *etc*. As a first assessment of bio-compatibility, we studied the influence of the nanogels on cell viability using tetrazolium dye (MTT) assay on HeLa cells (Fig. S13†). After 48 hours of incubation of HeLa cells with the MNGs, half maximal inhibitory concentrations (IC50s) of around 0.1 mg mL^{-1} were obtained. These values reflect the low toxicity of magnetic nanogels based on ethylene glycol and silanized magnetite nanoparticles.[52]

MNG interaction with the cells was studied by means of confocal visualization. After 12 hours of incubation of HeLa cells with different amounts of SureBeads™, MNG, and MNG-Dox, all magnetic systems can be observed in the surroundings of the cell with no clear evidence of cell internalization and an obvious cell death induced by the drug-loaded system (Fig. S14†). To explore cell interaction, the cells were trypsinized, washed, and settled in a magnetic rack. The MNGs could be observed under the microscope after the washing step (Fig. S15†). The non-interacting control (SureBeads™) could not be observed under the same conditions. This made us think that a non-specific interaction between the MNGs and the cellular membrane was occurring. We relied on this interaction to help in the tumor accumulation of the MNGs and the subsequent triggered antitumoral therapy.

Consequently, we studied the potential of the MNGs for photothermally induced chemotherapy of cancer cells. Different amounts of MNGs or MNG-Dox (40% DLC) were added to HeLa cells in 96-well plates and concentrated on the surface of the cells using a magnet. Then, the whole plate was irradiated for 5 minutes with NIR light. However, an identically treated second plate was not irradiated and it served as a control. 24 h after treatment, a concentration-dependent decrease in cell viability approaching complete cell death was observed for the non-loaded MNGs (Fig. 4A) after irradiation. With this, we demonstrate the ability of the MNPs in the network as phototransducers that increase the local tempera-
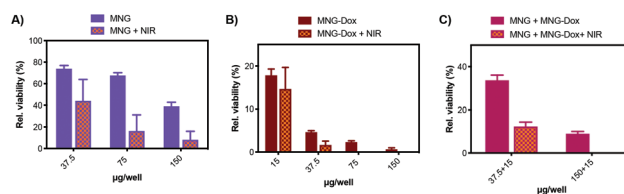

Fig. 4 Relative viabilities of HeLa cells 24 h after treatment with (A) MNGs, (B) MNG-DOX, and (C) a mixture of MNG-DOX and MNGs, with and without NIR irradiation for 5 minutes as calculated by ATP content.

ture sufficiently to enhance the cell death, making them suitable for NIR-triggered chemotherapy.

To analyze the NIR-triggered chemotherapeutic effect of both NIR irradiation and Dox activity, the cell viability of the nanogels loaded with Dox was tested with and without irradiation (Fig. 4B). Due to the high loading capacity of the MNGs, the cells treated with MNG-Dox already had a highly reduced viability of only about 20% without NIR irradiation, merely due to the chemotherapeutic effect of Dox. To make the NIR-triggered chemotherapeutic effect visible, we mixed MNG-Dox with the non-loaded MNGs, thereby reducing the drug concentration but keeping the amount of MNGs (the agent that produces heat upon irradiation) similar and repeated the irradiation experiment (Fig. 4C). Without irradiation, this mixture reduced the cell viability to about 40%, due to the intrinsic inhibitory activity of Dox. After irradiation, the cell viability decreased to 16% using 37.5 μg of MNG-Dox and 15 μg of MNG and decreased to complete cell death at higher concentrations (150 μg of MNG-Dox and 15 μg MNG), clearly demonstrating the NIR-triggered chemotherapeutic effect. It is worth mentioning that such promising results were achieved by NIR irradiation for only 5 minutes, whereas when employing an alternating magnetic field, a 2 h exposure was needed as reported.[58]

NIR-triggered chemotherapy evaluation *in vivo*

Considering the promising results *in vitro*, we became interested in investigating their potential for heat-mediated chemotherapy *in vivo*. First, the maximum tolerated dose of the MNGs was studied in healthy NMRI nude mice to evaluate sufficient doses and short-term toxicity. Five doses with increasing amounts of MNG (10, 20, 40, 70, and 100 mg kg^{-1}) were injected intravenously through the tail vein and the mice were observed for 15 days. Since there were no signs of compound-related toxicity, five extra injections of 100 mg kg^{-1} were performed for five consecutive days to reach a total accumulated dose of 500 mg kg^{-1}. One group of mice was sacrificed after the last treatment, and a second group was kept for another 13 days without showing signs of toxicity or body weight loss (Fig. 5A). In addition, the general behaviour of mice was not altered, indicating a good tolerability to the treatments.

Selected organs were collected (the liver, lung, spleen, kidneys, heart) and prepared for histopathological examin-

ation. The sections showed no specific toxicity-related alterations (Fig. 6). Particle accumulation was visible in the sections of the liver and spleen; however, apart from a slight dark staining of the liver, the mice did not show macroscopically obvious discoloration of the other organs or skin. In agreement with this, biodistribution measured by MRI showed the accumulation of MNGs mainly in the liver and kidneys and smaller amounts of the nanogels were detected in the spleen, lungs, and heart (Fig. S16 and S17†). Regarding the degradation and excretion of MNGs, we speculate that the degradation of our system will be highly comparable to those of other OEG-based nanogels since the thermoresponsive polymer is the most enzyme reactive component.[67] It is expected that the magnetic nanoparticles will be excreted based on related reports of magnetic nanoparticles.[68] We further studied the accumulation (which we expect *via* EPR) of the magnetic nanocarriers in A549 xenograft tumors in nude mice. Doses of 100 mg kg^{-1} were injected intravenously, and
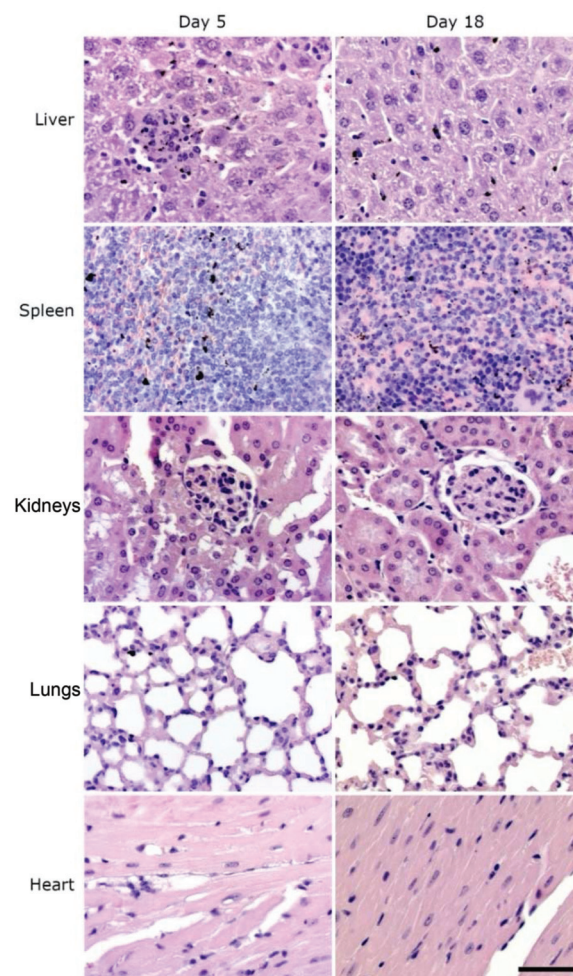
Fig. 6 Paraffin-embedded formalin fixed H&E stained sections of the selected organs of healthy mice treated with 100 mg kg^{-1} of MNGs 1× daily for 5 days. Left: after day 5 and right: after day 18. Scale bar = 50 μm.
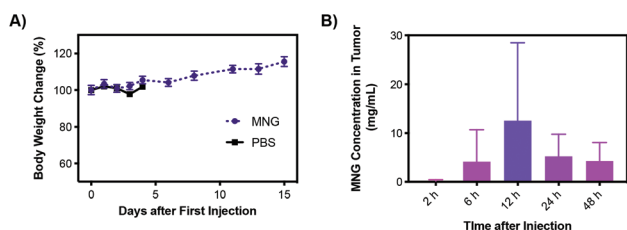
Fig. 5 (A) Body weight change for mice treated with MNGs five times with the maximum tolerable dose of 100 mg kg^{-1}. (B) Accumulation of MNGs in the tumor at different time points determined using MRI.

different groups of mice were sacrificed after 2, 6, 12, 24, and 48 h. The tumors were collected and fixed in 1% agarose gel for the quantification of MNGs by magnetic resonance imaging (Fig. 5B and S18†). A homogeneous distribution of the MNGs over the tumor volume was observed and a higher concentration could be observed in the more vascularized areas (Fig. S18†). A maximum mean MNG concentration of 12.3 mg mL^{-1} was accumulated 12 h after injection and reduced after that time point. Hence, we determined the optimal time window for therapeutic NIR irradiation after intravenous injection to be 12 h.

MNG and MNG-Dox were injected intravenously (i.v.) in A549 xenograft tumor bearing mice at doses of 100 mg kg^{-1}. 12 h after injection, the tumor was irradiated once for 5 min (following our findings in the *in vitro* release studies) with a 785 nm laser (500 mW) from a distance of 5 cm. The mice were monitored for a further 23 days and the tumor volume was measured twice per week (Fig. 7A, individual curves are depicted in Fig. S19†). Mice injected with PBS solution were used as reference for untreated tumor growth. The MNGs interfered with the expected growth of the tumor, showing a less aggressive growth profile compared to PBS. Similar values were obtained while irradiating the tumors 12 h after the MNG injection (Fig. 7A). This observation reflected that the ablation damage produced by MNG heating was in this case neglectable. We target this MNG concentration window to observe the NIR-triggered enhanced chemotherapy without interferences from tumor ablation. Dox-loaded MNG (MNG-Dox) was compared to non-formulated Dox injection at known therapeutic concentrations for this particular *in vivo* setting.[69,70] As expected, almost no tumor growth was observed for Dox until day 24 after injection day. After this period, the relative tumor volume abruptly peaked up to values comparable with the non-treated tumors at day 3.

Dox-loaded nanogels acted in a slower and constant manner on tumor growth when the release was likely only triggered by the local pH value, showing less growth inhibition in the first 24 days but continued until day 34, where values lower than the ones reached by the non-loaded MNGs were observed. This trend was enhanced when MNG-Dox was irradiated with NIR light showing the benefit of combined pH and NIR triggered Dox release from the nanogels. To further under-stand the mode of action and efficacy of our system, we administered MNGs by a different route. Doses of 45 µL (16 mg mL^{-1}) of MNGs and MNG-Dox were injected intratumorously (i.t.) and instantly irradiated for 5 min similar to the previous experiments and the tumor volume was comparably screened (Fig. 7B, individual curves are depicted in Fig. S20†). Like in the i.v. administration, the MNGs showed a less aggressive tumor growth trend than the PBS control. However, upon NIR irradiation, the tumor volume curve reached higher values, comparable with the PBS ones. We speculate that a higher MNG concentration in the tumor site was able to produce enough heat that led to an increased blood flow and perfusion to the tumor, promoting the overall tumor growth.[71]

The effects of a higher MNG concentration were also observed for the experiments using Dox-loaded nanogels. The free Dox inhibition effects were overcome by MNG-Dox, showing no increase of the tumor volume until day 28. NIR application resulted in a lower inhibition in mid-term (days 21 to 31) possibly by the same effect discussed above for the non-loaded nanogels. However, long-term inhibition at day 34 reached values slightly lower than treatment without irradiation with the Dox-loaded system.

To assess one of the known side effects of chemotherapy, body weight changes in all mice were monitored for both i.v. and i.t. (Fig. S21A and B† respectively) treatments. All mice treated with MNG and MNG-Dox, as well as the controls (PBS with and without irradiation), did not show any reduction in the body weight. Only the group treated with free doxorubicin showed decreasing body weights due to the toxic effects of the drug itself.

Hence, these nanocarriers present a chemotherapeutic activity triggered by NIR light with only 5 minutes of exposure. In addition, similar or better results were observed compared to those for other dual-responsive systems such as temperature/redox-sensitive,[72] pH/redox dual responsive[73] nanogels, as well as for magnetic polymeric nanocarriers modified with targeting groups.[74,75]

Conclusions

In conclusion, we report a facile synthetic approach of thermo-responsive nanogels where magnetic nanoparticles are employed as covalent cross-linkers. This new covalent strategy prevents the leakage of the MNPs from the polymer network. A fine control of sizes and cloud point temperature was achieved by changing the amount of MNP@MEMO and the DEGMA : OEGMA ratio. MNGs retain the magnetization, relaxation, and phototransducing properties of their parent magnetic nanoparticles. Moreover, doxorubicin was encapsulated into the MNGs, finding encapsulations similar or even higher to similar reported systems. In addition, we proved that its release could be controlled either by pH or by external triggering with NIR light.

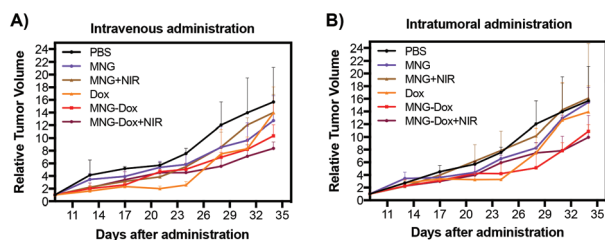We demonstrated the successful NIR-triggered chemo-therapy between local hyperthermia created by light-to-heat

Fig. 7 Relative tumor volume at different times after (A) intravenous and (B) intratumoral application of magnetic nanogels and treatment with and without NIR irradiation. PBS and free Dox were always administered intravenously.

conversion of the MNGs by NIR irradiation and the antiproliferative effect of doxorubicin *in vitro*. *In vivo* experiments were performed through intravenous and intratumoral administration. Intravenous administration revealed an NIR-triggered chemotherapeutic effect that improves Dox efficiency in tumor volume reduction, both in the mid term and in the long term. Tumor volume trends from intratumoral administration revealed a similar situation. However, we observed a tumor growth enhancing effect of the heat produced by the magnetic phototransducer. This comparative study reflects the importance of the correct dose and drug concentration in the administration of the NIR-triggered delivery system. Such factors are key for unleashing all the therapeutic potencies of the antitumoral modalities. In addition to their NIR-triggered chemotherapy capacity, it is worth mentioning that these hybrid nanogels can be used for photothermal therapy as well as for MRI, demonstrating their capacity as theranostic devices. It is important to highlight that this work paves the way for further clinical studies regarding the mechanisms that take place when injecting and irradiating these type of nanocarriers.

Conflicts of interest

There are no conflicts to declare.

Acknowledgements

References

1 M. Molina, M. Asadian-Birjand, J. Balach, J. Bergueiro, E. Miceli and M. Calderón, *Chem. Soc. Rev.*, 2015, **44**, 6161–6186.

2 S. S. Said, S. Campbell and T. Hoare, *Chem. Mater.*, 2019, **31**, 4971–4989.

3 H. S. El-Sawy, A. Al-Abd, T. Ahmed, K. M. El-Say and V. P. Torchilin, *ACS Nano*, 2018, **12**, 10636–10664.

4 G. Rimondino, C. Biglione, M. Martinelli, C. I. Alvarez Igarzabal and M. Strumia, in *Polymer Gels*, 2018, pp. 279–307.

5 S. Hajebi, N. Rabiee, M. Bagherzadeh, S. Ahmadi, M. Rabiee, H. Roghani-Mamaqani, M. Tahriri, L. Tayebi and M. R. Hamblin, *Acta Biomater.*, 2019, **92**, 1–18.

6 N. Vanparijs, L. Nuhn and B. G. De Geest, *Chem. Soc. Rev.*, 2017, **46**, 1193–1239.

7 S. Merino, C. Martín, K. Kostarelos, M. Prato and E. Vázquez, *ACS Nano*, 2015, **9**, 4686–4697.

8 T. Alejo, L. Uson and M. Arruebo, *J. Controlled Release*, 2019, **314**, 162–176.

9 N. D. Thorat, H. Townely, G. Brennan, A. K. Parchur, C. Silien, J. Bauer and S. A. M. Tofail, *ACS Biomater. Sci. Eng.*, 2019, **5**, 2669–2687.

10 A. Sneider, D. Vandyke, S. Paliwal and P. Rai, *Nanotheranostics*, 2017, **1**, 1–22.

11 V. Shanmugam, S. Selvakumar and C. S. Yeh, *Chem. Soc. Rev.*, 2014, **43**, 6254–6287.

12 J. Bergueiro and M. Calderón, *Macromol. Biosci.*, 2014, **15**, 183–199.

13 D. Jaque, L. Martínez Maestro, B. Del Rosal, P. Haro-Gonzalez, A. Benayas, J. L. Plaza, E. Martín Rodríguez and J. García Solé, *Nanoscale*, 2014, **6**, 9494–9530.

14 L. Jauffred, A. Samadi, H. Klingberg, P. M. Bendix and L. B. Oddershede, *Chem. Rev.*, 2019, **119**, 8087–9130.

15 H. Chen and Y. Zhao, *ACS Appl. Mater. Interfaces*, 2018, **10**, 21021–21034.

16 L. E. Theune, J. Buchmann, S. Wedepohl, M. Molina, J. Laufer and M. Calderón, *J. Controlled Release*, 2019, **311–312**, 147–161.

17 M. Asadian-Birjand, J. Bergueiro, S. Wedepohl and M. Calderón, *Macromol. Biosci.*, 2016, **16**, 1432–1441.

18 M. Molina, S. Wedepohl and M. Calderón, *Nanoscale*, 2016, **8**, 5852–58526.

19 F. Han, A. H. Soeriyadi, S. R. C. Vivekchand and J. J. Gooding, *ACS Macro Lett.*, 2016, **5**, 626–630.

20 W. T. Li, B. X. Xue, K. Shi, Y. Qu, B. Y. Chu and Z. Y. Qian, *Appl. Mater. Today*, 2019, **14**, 84–95.

21 S. M. Dadfar, K. Roemhild, N. I. Drude, S. von Stillfried, R. Knüchel, F. Kiessling and T. Lammers, *Adv. Drug Delivery Rev.*, 2019, **138**, 302–325.

22 C. Xu and S. Sun, *Adv. Drug Delivery Rev.*, 2013, **65**, 732–743.

23 H. Wang, G. Cao, Z. Gai, K. Hong, P. Banerjee and S. Zhou, *Nanoscale*, 2015, **7**, 7885–7895.

24 M. Moros, J. Idiago-lópez, L. Asín, E. Moreno-antolín, L. Beola, V. Grazú, R. M. Fratila, L. Gutiérrez and J. Martínez de la Fuente, *Adv. Drug Delivery Rev.*, 2019, **138**, 326–343.

25 S. Kossatz, J. Grandke, P. Couleaud, A. Latorre, A. Aires, K. Crosbie-Staunton, R. Ludwig, H. Dähring, V. Ettelt, A. Lazaro-Carrillo, M. Calero, M. Sader, J. Courty, Y. Volkov, A. Prina-Mello, A. Villanueva, Á. Somoza, A. L. Cortajarena, R. Miranda and I. Hilger, *Breast Cancer Res.*, 2015, **17**, 1–17.

26 O. Veiseh, J. W. Gunn and M. Zhang, *Adv. Drug Delivery Rev.*, 2010, **62**, 284–304.

27 T. K. Jain, J. Richey, M. Strand, D. L. Leslie-Pelecky, C. A. Flask and V. Labhasetwar, *Biomaterials*, 2008, **29**, 4012–4021.

28 F. Perton, M. Tasso, G. A. Muñoz Medina, M. Ménard, C. Blanco-Andujar, E. Portiansky, M. B. F. van Raap, D. Bégin, F. Meyer, S. Begin-Colin and D. Mertz, *Appl. Mater. Today*, 2019, **16**, 301–314.

29 L. Xiao, J. Li, D. F. Brougham, E. K. Fox, N. Feliu, A. Bushmelev, A. Schmidt, N. Mertens, F. Kiessling, M. Valldor, B. Fadeel and S. Mathur, *ACS Nano*, 2011, **5**, 6315–6324.

30 C. Biglione, J. Bergueiro, M. Asadian-Birjand, C. Weise, V. Khobragade, G. Chate, M. Dongare, J. Khandare, M. C. Strumia and M. Calderón, *Polymers*, 2018, **10**, 174–188.

31 M. Asadian-Birjand, C. Biglione, J. Bergueiro, A. Cappelletti, C. Rahane, G. Chate, J. Khandare, B. Klemke, M. C. Strumia and M. Calderón, *Macromol. Rapid Commun.*, 2016, **37**, 439–445.

32 V. Nandwana, S. R. Ryoo, T. Zheng, M. M. You and V. P. Dravid, *ACS Biomater. Sci. Eng.*, 2019, **5**, 3049–3059.

33 M. A. Macchione, C. Biglione and M. Strumia, *Polymers*, 2018, **10**, 527–561.

34 J. Liu, C. Detrembleur, A. Debuigne, M.-C. De Pauw-Gillet, S. S. Mornet, L. Vander Elst, S. Laurent, E. Duguet, C. Jerome and C. Jérôme, *J. Mater. Chem. B*, 2014, **2**, 1009–1023.

35 G. Liu, M. Cai, X. Wang, F. Zhou and W. Liu, *ACS Macro Lett.*, 2016, **5**, 144–148.

36 B. T. Mai, S. Fernandes, P. B. Balakrishnan and T. Pellegrino, *Acc. Chem. Res.*, 2018, **51**, 999–1013.

37 S. Backes, M. U. Witt, E. Roeben, L. Kuhrts, S. Aleed, A. M. Schmidt and R. Von Klitzing, *J. Phys. Chem. B*, 2015, **119**, 12129–12137.

38 A. Zhou, H. Luo, Q. Wang, L. Chen, T. C. Zhang and T. Tao, *RSC Adv.*, 2015, **5**, 15359–15365.

39 V. M. Vijayan, A. E. Beeran, S. J. Shenoy, J. Muthu and V. Thomas, *ACS Appl. Bio Mater.*, 2019, **2**, 757–768.

40 D. Zhao, X. Li, X. Shi, K. Ye, W. Liu and X. Lu, *RSC Adv.*, 2016, **6**, 61001–61005.

41 H. Yao, X. Li, X. Shi, G. Qiu and X. Lu, *Polym. Adv. Technol.*, 2019, **30**, 312–319.

42 T. Chen, Z. Cao, X. Guo, J. Nie, J. Xu, Z. Fan and B. Du, *Polymer*, 2011, **52**, 172–179.

43 R. Messing, N. Frickel, L. Belkoura, R. Strey, H. Rahn, S. Odenbach and A. M. Schmidt, *Macromolecules*, 2011, **44**, 2990–2999.

44 J. Liu, C. Detrembleur, S. Mornet, C. Jérôme and E. Duguet, *J. Mater. Chem. B*, 2015, **3**, 6117–6147.

45 C. Biglione, A. Sousa-Herves, M. Menger, S. Wedepohl, M. Calderón and M. C. Strumia, *RSC Adv.*, 2015, **5**, 15407–15413.

46 J. F. Lutz, K. Weichenhan, Ö. Akdemir and A. Hoth, *Macromolecules*, 2007, **40**, 2503–2508.

47 G. Vancoillie, D. Frank and R. Hoogenboom, *Prog. Polym. Sci.*, 2014, **39**, 1074–1095.

48 J.-F. Lutz, *J. Polym. Sci., Part A: Polym. Chem.*, 2008, **46**, 3459–3470.

49 M. M. Ali and H. D. H. Stoever, *Macromolecules*, 2004, **37**, 5219–5227.

50 S. Sugihara, S. Kanaoka and S. Aoshima, *Macromolecules*, 2005, **38**, 1919–1927.

51 M. Molina, S. Wedepohl, E. Miceli and M. Calderón, *Nanomedicine*, 2017, **12**, 117–129.

52 Z. Ferjaoui, E. Jamal Al Dine, A. Kulmukhamedova, L. Bezdetnaya, C. Soon Chang, R. Schneider, F. Mutelet, D. Mertz, S. Begin-Colin, F. Quilès, E. Gaffet and H. Alem, *ACS Appl. Mater. Interfaces*, 2019, **11**, 30610–30620.

53 J. S. Basuki, L. Esser, P. B. Zetterlund, M. R. Whittaker, C. Boyer and T. P. Davis, *Macromolecules*, 2013, **46**, 6038–6047.

54 M. Boularas, E. Gombart, J.-F. Tranchant, L. Billon and M. Save, *Macromol. Rapid Commun.*, 2015, **36**, 79–83.

55 Y. Oz, M. Arslan, T. N. Gevrek, R. Sanyal and A. Sanyal, *ACS Appl. Mater. Interfaces*, 2016, **8**, 19813–19826.

56 X. Lu, R. Jiang, Q. Fan, L. Zhang, H. Zhang, M. Yang, Y. Ma, L. Wang and W. Huang, *J. Mater. Chem.*, 2012, **22**, 6965–6973.

57 B. T. Mai, P. B. Balakrishnan, M. J. Barthel, F. Piccardi, D. Niculaes, F. Marinaro, S. Fernandes, A. Curcio, H. Kakwere, G. Autret, R. Cingolani, F. Gazeau and T. Pellegrino, *ACS Appl. Mater. Interfaces*, 2019, **11**, 5727–5739.

58 E. Cazares-Cortes, A. Espinosa, J. M. Guigner, A. Michel, N. Griffete, C. Wilhelm and C. Ménager, *ACS Appl. Mater. Interfaces*, 2017, **9**, 25775–25788.

59 M. Boularas, E. Deniau-Lejeune, V. Alard, J.-F. Tranchant, M. Save and L. Billon, *Polym. Chem.*, 2015, **7**, 350–363.

60 J. F. Lutz and A. Hoth, *Macromolecules*, 2006, **39**, 893–896.

61 I. Hilger and W. A. Kaiser, *Nanomedicine*, 2012, **7**, 1443–1459.

62 H. Chen, J. Burnett, F. Zhang, J. Zhang, H. Paholak and D. Sun, *J. Mater. Chem. B*, 2014, **2**, 757–765.

63 B. Sivakumar, R. G. Aswathy, R. Romero-Aburto, T. Mitcham, K. A. Mitchel, Y. Nagaoka, R. R. Bouchard, P. M. Ajayan, T. Maekawa and D. N. Sakthikumar, *Biomater. Sci.*, 2017, **5**, 432–443.

64 I. F. Tannock and D. Rotin, *Cancer Res.*, 1989, **49**, 4373–4384.

65 *Strategies to Modify the Drug Release from Pharmaceutical Systems*, ed. M. L. Bruschi, Woodhead Publishing, 2015, pp. 63–86.

66 R. W. Korsmeyer, R. Gurny, E. Doelker, P. Buri and N. A. Peppas, *Int. J. Pharm.*, 1983, **15**, 25–35.

67 Z. Jiang, Z. Zhu, C. Liu, Y. Hu, W. Wu and X. Jiang, *Polymer*, 2008, **49**, 5513–5519.

68 M. Longmire, P. L. Choyke and H. Kobayashi, *Nanomedicine*, 2008, **3**, 703–717.

69 L. D. Mayer, L. C. L. Tai, D. S. C. Ko, D. Masin, R. S. Ginsberg, P. R. Cullis and M. B. Bally, *Cancer Res.*, 1989, **49**, 5922–5930.

70 A. Cabanes, D. Tzemach, D. Goren, A. T. Horowitz and A. Gabizon, *Clin. Cancer Res.*, 1998, **4**, 499–505.

71 E. A. Repasky, S. S. Evans and M. W. Dewhirst, *Cancer Immunol. Res.*, 2013, **1**, 210–217.

72 F. Li, H. Yang, N. Bie, Q. Xu, T. Yong, Q. Wang, L. Gan and X. Yang, *ACS Appl. Mater. Interfaces*, 2017, 23564–23573.

73 H. Yang, Q. Wang, S. Huang, A. Xiao, F. Li, L. Gan and X. Yang, *ACS Appl. Mater. Interfaces*, 2016, **8**, 7729–7738.

74 X. Sun, R. Du, L. Zhang, G. Zhang, X. Zheng, J. Qian, X. Tian, J. Zhou, J. He, Y. Wang, Y. Wu, K. Zhong, D. Cai, D. Zou and Z. Wu, *ACS Nano*, 2017, **11**, 7049–7059.

75 Z. Zhang and S. Song, *Biomaterials*, 2017, **132**, 16–27.